J|A|C|S ARTICLES

Published on Web 10/06/2010

Chalcogels: Porous Metal−Chalcogenide Networks from Main-Group Metal Ions. Effect of Surface Polarizability on Selectivity in Gas Separation

Santanu Bag[†] and Mercouri G. Kanatzidis*[,†,‡]

Department of Chemistry, Northwestern University, Evanston, Illinois 60208, United States, and Materials Science Division, Argonne National Laboratory, Argonne, Illinois 60439, United States

Received July 5, 2010; E-mail: m-kanatzidis@northwestern.edu

Abstract: We report the synthesis of metal−chalcogenide gels and aerogels from anionic chalcogenide clusters and linking metal ions. Metal ions such as Sb^{3+} and Sn^{2+}, respectively chelated with tartrate and acetate ligands, react in solution with the chalcogenide clusters to form extended polymeric networks that exhibit gelation phenomena. Chalcogenide cluster anions with different charge densities, such as $[Sn_2S_6]^{4-}$ and $[SnS_4]^{4-}$, were employed. *In situ* rheological measurements during gelation showed that a higher charge density on the chalcogenide cluster favors formation of a rigid gel network. Aerogels obtained from the gels after supercritical drying have BET surface areas from 114 to 368 m^2/g. Electron microscopy images coupled with nitrogen adsorption measurements showed the pores are micro (below 2 nm), meso (2−50 nm), and macro (above 50 nm) regions. These chalcogels possess band gaps in the range of 1.00−2.00 eV and selectively adsorb polarizable gases. A 2-fold increase in selectivity toward CO_2/C_2H_6 over H_2 was observed for the $Pt/Sb/Ge_4Se_{10}$-containing aerogel compared to aerogel containing $Pt_2Ge_4S_{10}$. The experimental results suggest that high selectivity in gas adsorption is achievable with high-surface-area chalcogenide materials containing heavy polarizable elements.

Introduction

Aerogels are a unique class of porous materials with low densities, large open pores of all sizes, and high internal surface area. They derive from gel networks consisting of interconnected nanosized building units. They are extensively studied for applications in catalysis, electronics, thermal insulation, sensors, ceramics, cosmic dust collectors, optical films, and chromatographic molecular separations and for the easy generation of monoliths.[1] The great preponderance of aerogels are based on metal oxides, with the traditional SiO_2, Al_2O_3, and TiO_2 being the prime targets of decade-long investigations.[2−4] These aerogels are either insulators or wide-band-gap semiconductors. The development of porous, narrow energy band gap aerogel materials is still in its infancy.[5] Chalcogenide gels and aerogels from several binary metal sulfide systems (e.g., GeS_2, ZnS, CdS, TiS_2, NbS_2, La_2S_3, and WS_x) have successfully been made.[6−10] The combination of electronic properties inherent in inorganic chalcogenides with the availability of large surface areas and open cavities could lead to new functionalities in porous materials.[11] Well-defined metal−chalcogenide molecular building units such as $[M_4Q_{10}]^{4-}$, $[M_2Q_6]^{4-}$, and $[MQ_4]^{4-}$ were previously used to construct mesostructured chalcogenide materials.[12−29] However, attempts to convert those into real porous structures by removing the surfactants residing in the pores were unsuccessful. Therefore, an alternate sol−gel strategy was devised, and highly porous chalcogenide aerogels were obtained.[6]

Recently, we described the chalcogels as a new class of aerogels made from platinum and germanium and chalcogens (the column of elements on the periodic table beginning with but not including oxygen) such as sulfur, selenium, and tellurium.[6,30] The platinum-based chalcogels preferentially absorb heavy metals, showing promise for absorbing pollutants such as mercury from water. The synthetic strategy was further extended to produce tetrathiomolybdate(tungstate)-based chalcogels.[7] The highly porous aerogels made of Co(Ni)−Mo(W)−S chalcogels showed enhanced catalytic activity for the hydrodesulfurization of thiophenes.[7] The type of chemistry employed to construct these chalcogels is fundamentally different from the self-polymerization pathway of silicate systems, where first hydrolysis of the silicate precursor occurs followed by condensation of $[SiO_4]^{4-}$ units.[1] The generation of metal−chalcogenide binary gels such as GeS_2 involves thiolysis reactions, where bubbling of H_2S is required,[31] whereas the CdS and CdSe

[†] Northwestern University.
[‡] Argonne National Laboratory.

(1) Husing, N.; Schubert, U. *Angew. Chem., Int. Ed.* **1998**, *37*, 23–45.
(2) Gesser, H. D.; Goswami, P. C. *Chem. Rev.* **1989**, *89*, 765–788.
(3) Teichner, S. J.; Nicolaon, G. A.; Vicarini, M. A.; Gardes, G. E. E. *Adv. Colloid Interface Sci.* **1976**, *5*, 245–273.
(4) Zhu, Z.; Lin, M.; Dagan, G.; Tomkiewicz, M. *J. Phys. Chem.* **1995**, *99*, 15950–15954.
(5) Bag, S.; Arachchige, I. U.; Kanatzidis, M. G. *J. Mater. Chem.* **2008**, *18*, 3628–3632.
(6) Bag, S.; Trikalitis, P. N.; Chupas, P. J.; Armatas, G. S.; Kanatzidis, M. G. *Science* **2007**, *317*, 490–493.
(7) Bag, S.; Gaudette, A. F.; Bussell, M. E.; Kanatzidis, M. G. *Nat. Chem.* **2009**, *1*, 217–224.
(8) Mohanan, J. L.; Arachchige, I. U.; Brock, S. L. *Science* **2005**, *307*, 397–400.
(9) Brock, S. L.; Arachchige, I. U.; Kalebaila, K. K. *Comments Inorg. Chem.* **2006**, *27*, 103–126.
(10) Arachchige, I. U.; Brock, S. L. *Acc. Chem. Res.* **2007**, *40*, 801–809.
(11) Kanatzidis, M. G. *Adv. Mater.* **2007**, *19*, 1165–1181.

Table 1. Energy Gap and Nitrogen Physisorption Data for Metal−Chalcogenide Aerogels

chalcogel	linker	building unit	band gap (eV); BET surface area (m^2/g)	adsorption total pore volume, V_p (cm^3/g)[a]	limiting micropore volume, V_o (cm^3/g)[b]	microporosity (%)[c]
Chalcogel-Sb-1	Sb^{3+}	$[SnS_4]^{4-}$	1.88; 240	1.53	0.09	5.8
Chalcogel-Sb-2	Sb^{3+}	$[SnSe_4]^{4-}$	1.30; 114	0.36	0.04	11.1
Chalcogel-Sb-3	Sb^{3+}	$[Sn_2Se_6]^{4-}$	1.33; 200	0.57	0.07	12.7
Chalcogel-Sb-4	Sb^{3+}	$[SbSe_4]^{3-}$	1.30; 127	0.20	0.04	20.0
Chalcogel-PtSb-1	Sb^{3+}, Pt^{2+}	$[Ge_4Se_{10}]^{4-}$	1.36; 226	0.60	0.07	11.7
Chalcogel-Sn-1	Sn^{2+}	$[SnS_4]^{4-}$	1.65; 210	0.67	0.07	10.5
Chalcogel-Sn-2	Sn^{2+}	$[Sn_2S_6]^{4-}$	1.00, 2.00; 368	1.16	0.11	9.5

[a] Adsorption total pore volume is measured at relative pressure (P/P_o) of 0.97. [b] Limiting micropore volume is obtained in the relative pressure region of $5 \times 10^{-6}-2 \times 10^{-2}$. [c] Percentage microporosity is obtained by using the equation $(V_{o,N_2}/V_p) \times 100$.

Table 2. Elemental Composition of Chalcogels

chalcogel	linker	building unit	time required to get rigid gel (days)	solution color upon mixing	color of gel	elemental composition
Chalcogel-Sb-1	Sb^{3+}	$[SnS_4]^{4-}$	10	yellow	orange brown	$Sb_{2.5}SnS_{3.4}$[a]
Chalcogel-Sb-2	Sb^{3+}	$[SnSe_4]^{4-}$	14	dark brown	brownish black	$Sb_{2.4}SnSe_{3.6}$[b]
Chalcogel-Sb-3	Sb^{3+}	$[Sn_2Se_6]^{4-}$	14	dark brown	brownish black	$Sb_{2.5}SnSe_{3.7}$[b]
Chalcogel-Sb-4	Sb^{3+}	$[SbSe_4]^{3-}$	10	dark brown	brownish black	$SbSe_{1.8}$[b]/$SbSe_{1.5}$[c]
Chalcogel-PtSb-1	Sb^{3+}, Pt^{2+}	$[Ge_4Se_{10}]^{4-}$	21	dark brown	brownish black	$Pt_{0.4}Sb_{0.8}GeSe_{2.8}$[c]
Chalcogel-Sn-1	Sn^{2+}	$[SnS_4]^{4-}$	21	orange	dark brown	$SnS_{1.5}$[c]
Chalcogel-Sn-2	Sn^{2+}	$[Sn_2S_6]^{4-}$	30	orange	dark brown	$SnS_{1.6}$[c]

[a] X-ray fluorescence (XRF) data. [b] Inductively coupled plasma (ICP) analysis data. [c] X-ray energy dispersive spectroscopy (XEDS) data.

nanocrystal-based gels are generated upon surface oxidation of their capping agents.[10] In contrast, in our synthetic scheme, chalcogenide building units such as $[M_4Q_{10}]^{4-}$, $[M_2Q_6]^{4-}$, and $[MQ_4]^{4-}$ are joined together with linking metal ions to form random three-dimensional interconnected frameworks.

The key event that needs to occur in order to obtain aerogels is gelation in solution. With chalcogenides, however, gelation is difficult, as more often, rapid precipitation occurs. Because of the slow ligand substitution kinetics of Pt^{2+}, the random polymerization reaction is slow enough to ensure gelation and avoid precipitation.[6] We have now broadened the scope of this chemistry to include less expensive linking metals, which we show can also achieve gelation. We demonstrate the general nature of chalcogels as a broad class of chalcogenide materials. Namely, we report a nonaqueous room-temperature synthetic route to chalcogels starting from simple molecular building units $[M_2Q_6]^{4-}$, $[MQ_4]^{4-}$, and $[MQ_4]^{3-}$, with Sb^{3+} and Sn^{2+} as linking metal ions. Because of the different charge densities of these anions, which can be in equilibrium in solution,[9] we can expect different rigidities in the assembled frameworks. We also report for the first time preliminary *in situ* rheological measurements made during the gelation process and correlate the charge density of the starting inorganic building unit to the structural rigidity of the final chalcogel. Finally, we report gas adsorption studies using CO_2, C_2H_6, CH_4, and H_2 on two selected chalcogel samples, and we show remarkable selectivity that is based on the polarizability of the atomic components in the inorganic framework. Rather than pore size and shape, it is the high polarizability of the chalcogenide framework that controls the selectivity factor. These results suggest that the chalcogenide-based aerogel materials could play an important role in membrane separation processes for the purification of gases.

Experimental Section

General Methods. The starting metal salts $K_2(SbC_4H_2O_6)_2 \cdot 3H_2O$ and $(C_2H_3O_2)_2Sn$(II) and solvent like formamide used in this synthesis were purchased from Alfa Aesar. $Na_4SnS_4 \cdot 14H_2O$,[32] $Na_4Sn_2S_6 \cdot 14H_2O$,[33] K_4SnSe_4,[34] $K_4Sn_2Se_6$,[35] and K_3SbSe_4[36] were freshly prepared according to literature procedures. The syntheses of all chalcogels reported here were done in formamide solution in an inert N_2-filled glovebox at room temperature. Solvents (including

(12) Bag, S.; Kanatzidis, M. G. *J. Am. Chem. Soc.* **2008**, *130*, 8366–8376.
(13) Trikalitis, P. N.; Rangan, K. K.; Bakas, T.; Kanatzidis, M. G. *Nature* **2001**, *410*, 671–675.
(14) Trikalitis, P. N.; Rangan, K. K.; Kanatzidis, M. G. *J. Am. Chem. Soc.* **2002**, *124*, 2604–2613.
(15) Trikalitis, P. N.; Rangan, K. K.; Bakas, T.; Kanatzidis, M. G. *J. Am. Chem. Soc.* **2002**, *124*, 12255–12260.
(16) Trikalitis, P. N.; Ding, N.; Malliakas, C.; Billinge, S. J. L.; Kanatzidis, M. G. *J. Am. Chem. Soc.* **2004**, *126*, 15326–15327.
(17) Trikalitis, P. N.; Bakas, T.; Papaefthymiou, V.; Kanatzidis, M. G. *Angew. Chem., Int. Ed.* **2000**, *39*, 4558–4562.
(18) Trikalitis, P. N.; Bakas, T.; Kanatzidis, M. G. *J. Am. Chem. Soc.* **2005**, *127*, 3910–3920.
(19) Trikalitis, P.; Rangan, K. K.; Kanatzidis, M. G. *Mater. Res. Soc. Symp.* **2002**, *703*, 1–6.
(20) Ding, N.; Takabayashi, Y.; Solari, P. L.; Prassides, K.; Pcionek, R. J.; Kanatzidis, M. G. *Chem. Mater.* **2006**, *18*, 4690–4699.
(21) Rangan, K. K.; Billinge, S. J. L.; Petkov, V.; Heising, J.; Kanatzidis, M. G. *Chem. Mater.* **1999**, *11*, 2629–2632.
(22) Rangan, K. K.; Trikalitis, P. N.; Bakas, T.; Kanatzidis, M. G. *Chem. Commun.* **2001**, 809–810.
(23) Rangan, K. K.; Trikalitis, P. N.; Canlas, C.; Bakas, T.; Weliky, D. P.; Kanatzidis, M. G. *Nano Lett.* **2002**, *2*, 513–517.
(24) Rangan, K. K.; Trikalitis, P. N.; Kanatzidis, M. G. *J. Am. Chem. Soc.* **2000**, *122*, 10230–10231.
(25) MacLachlan, M. J.; Coombs, N.; Ozin, G. A. *Nature* **1999**, *397*, 681–684.
(26) MacLachlan, M. J.; Coombs, N.; Bedard, R. L.; White, S.; Thompson, L. K.; Ozin, G. A. *J. Am. Chem. Soc.* **1999**, *121*, 12005–12017.
(27) Riley, A. E.; Korlann, S. D.; Richman, E. K.; Tolbert, S. H. *Angew. Chem., Int. Ed.* **2006**, *45*, 235–241.
(28) Riley, A. E.; Tolbert, S. H. *J. Am. Chem. Soc.* **2003**, *125*, 4551–4559.
(29) Korlann, S. D.; Riley, A. E.; Kirsch, B. L.; Mun, B. S.; Tolbert, S. H. *J. Am. Chem. Soc.* **2005**, *127*, 12516–12527.
(30) Kanatzidis, M. G.; Bag, S. U.S. Patent 7,727,506.
(31) Kalebaila, K. K.; Georgiev, D. G.; Brock, S. L. *J. Non-Cryst. Solids* **2006**, *352*, 232–240.
(32) Schiwy, V. W.; Pohl, S.; Krebs, B. *Z. Anorg. Allg. Chem.* **1973**, *402*, 77.
(33) Krebs, B.; Pohl, S.; Schiwy, W. *Z. Anorg. Allg. Chem.* **1972**, *393*, 241–252.
(34) Klepp, K. O. *Z. Naturforsch., B: Chem. Sci.* **1992**, *47*, 411.
(35) Eisenmann, B.; Hansa, J. *Z. Kristallogr.* **1993**, *203*, 299.
(36) Eisenmann, B.; Zagler, R. *Z. Naturforsch. Teil B.* **1989**, *44*, 249–256.

ethanol and water, which were used for the solvent-exchange process) were deoxygenated by bubbling N_2 through them for about 1 h before taking them into the glovebox.

Synthesis of Sb-Linked Chalcogels. Chalcogel names are based on the linking metal ion and are listed in Table 1.

A gel using Sb^{3+} as linking metal was prepared in formamide. For a typical synthesis of Chalcogel-Sb-1, $Na_4SnS_4 \cdot 14H_2O$ (0.059 g, 0.1 mmol) and $K_2(SbC_4H_2O_6)_2 \cdot 3H_2O$ (0.090 g, 0.135 mmol) were dissolved in hot (75 °C) formamide (2 mL) in separate vials with continuous shaking. The two solutions were then mixed together and shaken for 5 min. During this shaking, the color changed from yellow to orange and then to deep orange-red. This solution was then poured into a plastic Petri dish, covered, and left undisturbed for about 10 days. After several washings with a 50:50 (v/v) water−ethanol mixture, absolute ethanol was added and decanted four or five times over a couple of days. The resulting gel was then supercritically dried with liquid CO_2. The final aerogel product was orange-brown in color. A similar synthetic strategy was used for almost all chalcogel-Sb preparations, expect for the aging time. Some systems needed up to one month of aging for good mechanical stability of the gel networks (Table 2).

Synthesis of Sn-Linked Chalcogels. Chalcogel containing a Sn−S backbone was prepared using respective tin building units and tin(II) acetate salt [$Sn(CH_3CO_2)_2$]. As an example, for preparation of Chalcogel-Sn-2, $Na_4Sn_2S_6 \cdot 14H_2O$ (0.2 mmol) and tin acetate(II) (0.4 mmol) were dissolved in a total 8 mL of formamide in two separate vials. The tin(II) acetate solution was added very slowly to the $Na_4Sn_2S_6 \cdot 14H_2O$ solution with vigorous stirring. Small, colloidal-like yellowish-orange particles appeared upon addition of a drop of tin(II) acetate solution, but they disappeared with shaking. Addition of the tin(II) acetate continued with vigorous shaking. After addition of the tin(II) acetate was complete, the viscosity of the resulting solution increased rapidly within minutes. The resulting viscous solution was then poured onto a Petri dish and left undisturbed for 3−4 weeks. The resulting monolithic gel was subsequently washed with water and ethanol over 3 d and finally supercritically dried with liquid carbon dioxide, resulting in the aerogel. For Chalcogel-Sn systems, the elemental composition matches well with the starting stoichiometry from EDS results. Powder X-ray diffraction of Chalcogel-Sn-2 shows formation of Sn_2S_3 along with SnS_2 (see Supporting Information, Figure S1).

Synthesis of Chalcogel-PtSb-1. Synthesis of Chalcogel-PtSb-1 was done using $[Ge_4Se_{10}]^{4-}$ building units. $(TMA)_4Ge_4Se_{10}$ (where TMA is the tetramethylammonium cation) (0.1 mmol), K_2PtCl_4 (0.1 mmol), and $K_2(SbC_4H_2O_6)_2 \cdot 3H_2O$ were dissolved in three separate vials using a total volume of 7 mL of formamide. The solutions of platinum and antimony salt were then added dropwise at the same time to the $[Ge_4Se_{10}]^{4-}$ solution. The resulting sol was left undisturbed for about 3 weeks to become a monolithic gel and then subsequently washed with a 50:50 water−ethanol mixture and absolute ethanol several times. The final "alcogel" (gel filled with alcohol)[37] was supercritically dried to yield a spongy aerogel.

Physical Measurements. Scanning Electron Microscopy (SEM), Transmission Electron Microscopy (TEM), X-ray Fluorescence (XRF), Infrared Spectroscopy (IR), and Thermogravimetric Analysis (TGA). SEM images of the aerogel samples were taken with a Hitachi S-4800N variable-pressure scanning electron microscope (VP-SEM). Powdered aerogel samples were gently placed on carbon tape, sputter-coated with gold, and taken into the instrument chamber for image capture. TEM samples were prepared by suspending the aerogel sample in ether and then casting on a holey carbon-coated Cu grid. High-resolution TEM was done with a JEOL 2100F instrument (field emission) operating at 200 kV. FT-IR spectra were recorded on a Nicolet 750 Magna-IR series II spectrometer with 2 cm^{-1} resolution. Thermogravimetric analyses were performed using a computer-controlled Shimadzu TGA-50 analyzer. Typically, 20 mg of sample was placed in a silica bucket and heated in a nitrogen flow of 50 mL/min with a rate of 10 °C/min.

Elemental Analysis. For quantitative microprobe analyses, X-ray energy-dispersive spectroscopy (EDS) was performed using a Hitachi S-3400N VP-SEM equipped with a Noran EDS detector. Data acquisition was performed several times in different areas of flat surfaces of aerogel pellet samples using an accelerating voltage of 25 keV and 120-s accumulation time. Elemental analysis of the title chalcogel-Sb samples showed an anomalous composition. Since the antimony (L) and tin (L) X-ray fluorescence lines are very close (3.6 and 3.44 keV, respectively) in the EDS spectrum, quantification is difficult for Sb- and Sn-containing samples. Attempts to quantify elements by inductively coupled plasma (ICP-AES) analysis often failed due to loss of sulfur or tin during sample preparation by acid dissolution. Thus, elemental analysis for sulfur-containing samples by the ICP method is not reliable. Hence, XRF measurement was done for Chalcogel-Sb-1. X-ray fluorescence spectrometry is a technique similar to SEM-EDS, except for the source of radiation. In XRF, an X-ray beam is the source of radiation instead of an electron beam. XRF is a complementary method to SEM-EDS and more sensitive for elements of high atomic weights.[38] Analytical XRF measurements were done on an aerogel pellet sample using a Bruker AXS S4 explorer X-ray spectrometer under a helium environment.

Band Gap Measurements. UV/vis/near-IR diffuse reflectance spectra were obtained at room temperature on a Shimadzu UV-3010 PC double-beam, double-monochromator spectrophotometer in the wavelength range of 200−2500 nm. $BaSO_4$ powder was used as a reference (100% reflectance) and base material on which the powder sample was coated. The reflectance data were converted to absorption using the Kubelka−Munck function, and the band edge for each sample was estimated from the intercept of the line extrapolated from the high-energy end of the absorption to the baseline.[39]

Rheological Study. Rheological measurements were performed with an ARES-LS strain-controlled rheometer in a cone−plate geometry with a 0.048 mm gap. *In situ* measurements were done at 2% strain with a frequency of 10 rad/s. For each oscillatory shear experiment, the applied strain was maintained at a constant nominal value (1%) within the linear viscoelastic range, determined with the aid of strain sweeps. The studied solution concentrations were same as in the synthetic procedure (0.1 mmol of $Na_4SnS_4 \cdot 14H_2O$ and 0.135 mmol of $K_2(SbC_4H_2O_6)_2 \cdot 3H_2O$ in a total of 4 mL of formamide; also 0.1 mmol of $Na_4Sn_2S_6 \cdot 14H_2O$ and 0.135 mmol of $K_2(SbC_4H_2O_6)_2 \cdot 3H_2O$ in a total of 4 mL of formamide). The characteristic viscoelastic functions,[40] storage modulus (G'), loss modulus (G''), and complex viscosity (η^*), have been obtained at 25 °C.

Pair Distribution Function (PDF) Analysis. Diffraction experiments for PDF analysis were performed at the Advanced Photon Source located at Argonne National Laboratory, Argonne, IL, using high-energy X-rays with the powder samples packed in a 1 mm Kapton capillary. For data collection, an X-ray energy of 77.528 keV ($\lambda = 0.15992$ Å) was used to record diffraction patterns to high values of momentum transfer while eliminating fluorescence from the sample. The two-dimensional images were integrated within Fit 2D to obtain the one-dimensional powder diffraction pattern, masking areas obscured by the beam stop arm. The PDFs, $G(r) = 4\pi r[\rho(r) - \rho_o]$, where $\rho(r)$ and ρ_o are the instantaneous

(37) Brinker, C. J.; Scherer, G. W. *The Physics and Chemistry of Sol-Gel Processing*; Academic Press: San Diego, CA, 1990.

(38) Beckhoff, B.; Kanngiefer, B.; Langhoff, N.; Wedell, R.; Wolff, H. *Handbook of practical X-ray fluorescence analysis*; Springer: Berlin, 2006.

(39) Mccarthy, T. J.; Ngeyi, S. P.; Liao, J. H.; Degroot, D. C.; Hogan, T.; Kannewurf, C. R.; Kanatzidis, M. G. *Chem. Mater.* **1993**, 5, 331–340.

(40) Macosko, C. W. *Rheology: Principles, Measurements, and Applications*; Wiley-VCH: New York, 1994.

and average densities, were extracted using PDFgetX2,[41] subtracting the contributions from the sample environment and background to the measured diffraction intensities. Corrections for multiple scattering, X-ray polarization, sample absorption, and Compton scattering were then applied to obtain the structure function, $S(Q)$. Direct Fourier transform of the reduced structure function, $F(Q) = Q[S(Q) - 1]$, yielded $G(r)$, the PDF as described previously.[42]

Supercritical Drying. Critical-point drying (CPD) of the chalcogels was done with a Bal-Tec CPD 030 (Balzers). Before the gel-filled, custom-built drying basket was placed into the CPD chamber, the chamber was purged a couple of times with N_2. In this supercritical drier, the sample was soaked with liquid carbon dioxide and flushed 15−18 times over a period of 8 h at 10 °C to completely exchange the ethanol from the material (typical for 10 cm^3 of gel sample). Depending on the amount of gel, the soaking time and exchange time vary. Finally, an aerogel was obtained after supercritical drying at 40 °C. (**Caution***: During supercritical drying, CO_2 gas should be vented off very slowly. Rapid CO_2 ventilation would cause collapse of the pore structure*.)

Density Measurements. The skeletal density of a representative aerogel material was measured by using a Micromeritics AccuPyc 1340 gas pycnometer (1 cm^3 model) using ultra-high-purity (UHP) helium gas. About 200 mg of sample was taken for measurement. Analysis run cycles were continued until a standard deviation of ±0.0002 cm^3 was obtained for the sample volume. Bulk density was measured by cutting a rectangular-shaped monolithic aerogel, measuring its dimensions by using slide calipers, and subsequently weighing the aerogel sample on an electronic balance (accurate up to 5 decimal places). Typical monolithic aerogel sample dimensions are 0.7 × 0.6 × 0.1 cm.

Nitrogen Physisorption Measurements. Nitrogen adsorption and desorption isotherms were measured at 77 K using liquid nitrogen on a Micromeritics ASAP 2020 system. For each measurement, about 200 mg of sample was taken. Before measurement, samples were degassed at 348 K under vacuum ($<10^{-4}$ mbar) overnight. Low-pressure incremental dosing of 3 cm^3/g(STP) and 45 s equilibration were applied as analysis conditions. BET transform plots were obtained in the 0.05−0.2 relative pressure (P/P_o) regions, and correlation coefficients of 0.99999 were obtained in each case.

Hydrogen, Carbon Dioxide, Ethane, and Methane Physisorption Measurements. All physisorption measurements were performed on a Micromeritics ASAP 2020 system. A cryogenic water bath (50:50 vol % water−ethylene glycol mixture) controlled by a NESLAB RTE10 Digital Plus (Thermo Electron Corp.) chiller system was used for each measurement. After free space measurement with He gas, the sample tube was evacuated manually at 348 K for 4 h to remove any trapped He. Low-pressure incremental dosing of 0.8 cm^3/g(STP) and 120 s of equilibration were employed for every analysis.

Inductively Coupled Plasma−Atomic Emission (Optical Emission) Spectroscopy [ICP-AES(OES)] Analysis. To determine the elemental compositions of chalcogel samples, powder aerogels were first suspended in water, and then aqua-regia was added slowly to the samples in closed volumetric flasks which were kept overnight for sonication until all solid was dissolved. These samples were diluted before the measurements so that their concentrations could fall within the range of calibration. For each chalcogel, samples from three different lots were analyzed independently to have better statistics of results.

Accurate determinations of Sn, Sb, and Se concentrations were performed by ICP-AES using a VISTA MPX CCD simultaneous ICP-OES instrument. Standards of the elements of interest were prepared by diluting commercial (Aldrich or GFS chemicals) 1000 ppm ICP standards of these elements. Ten calibration standards from 1 to 12 ppm were made. The calibration was linear, with errors around 3%. The ICP-AES intensity was the result of three 30-s exposures. For each sample, three readings of the ICP-AES intensity were recorded and averaged. The standards were reanalyzed after each analysis of the samples.

Gas Selectivity Using the Ideal Adsorbed Solution Theory (IAST) Approach.[43] The single-component adsorption isotherms were described by fitting the data with the following virial-type equation:[43]

$$p = \frac{\upsilon}{K}\exp(c_1\upsilon + c_2\upsilon^2 + c_3\upsilon^3 + c_4\upsilon^4) \quad \text{(i)}$$

where p is the pressure in Torr, υ is the amount adsorbed in mmol g^{-1}, K is the Henry constant in mmol g^{-1} $Torr^{-1}$, and c_i are the constants of the virial equation.

The free energy of desorption at a given value of temperature and pressure of the gas is obtained from the analytical integration of eq i:

$$G(T,p) = RT\int_0^p \frac{n}{p}\,dp = RT\left(\upsilon + \frac{1}{2}c_1\upsilon^2 + \frac{2}{3}c_2\upsilon^3 + \frac{3}{4}c_3\upsilon^4 + \frac{4}{5}c_4\upsilon^5\right) \quad \text{(ii)}$$

The free energy of desorption is a function of temperature and pressure, $G(T,p)$, and describes the minimum work (Gibbs free energy) that is required to completely degas the adsorbant surface. For a binary mixture of components i and j, eq ii yields the individual pure loadings, υ_i^0 and υ_j^0, at the same free energy of desorption:

$$G_i^0(\upsilon_i^0) = G_j^0(\upsilon_j^0) \quad \text{(iii)}$$

The partial pressure of components i and j in an ideal adsorption mixture can be given:

$$py_i = p_i^0(\upsilon_i^0)x_i \quad \text{(iv)}$$

$$py_j = p_j^0(\upsilon_j^0)x_j \quad \text{(v)}$$

where y_i (= 1 − y_j) and x_i (= 1 − x_j) are the molar fractions of component i in the gas phase and the adsorbed phase, respectively, and p_i^0 and p_j^0 are the pure component pressures of i and j, respectively.

After solving eqs iii−v and eq i, the selectivity for the adsorbates i and j ($s_{i,j}$) and the total pressure (p) of the gas mixture can be obtained from eqs vi and vii, respectively:

$$S_{i,j} = \frac{x_i/y_i}{x_j/y_j} = \frac{p_j^0}{p_i^0} \quad \text{(vi)}$$

$$p = \sum_i^j p_i^0 x_i \quad \text{(vii)}$$

Results and Discussion

Synthesis. In the present study, anionic chalcogenide clusters and chelated linking metal ions were dissolved separately in warm formamide and mixed at room temperature, forming a clear solution. The solution, when left undisturbed during aging, gradually increases its viscosity to form a rigid gel (see Table 2). For example, Chalcogel-Sb-1, Chalcogel-Sb-4, and Chalcogel-Sn-2 form according to eqs 1, 2, and 3, respectively. The

(41) Qiu, X.; Thompson, J. W.; Billinge, S. J. L. *J. Appl. Crystallogr.* **2004**, *37*, 678.

(42) Egami, T.; Billinge, S. J. L. *Underneath the Bragg Peaks: Structural Analysis of Complex Materials*; Pergamon Press: Amsterdam, 2003.

(43) Myers, A. L. *Adsorption−J. Int. Adsorpt. Soc.* **2003**, *9*, 9–16.

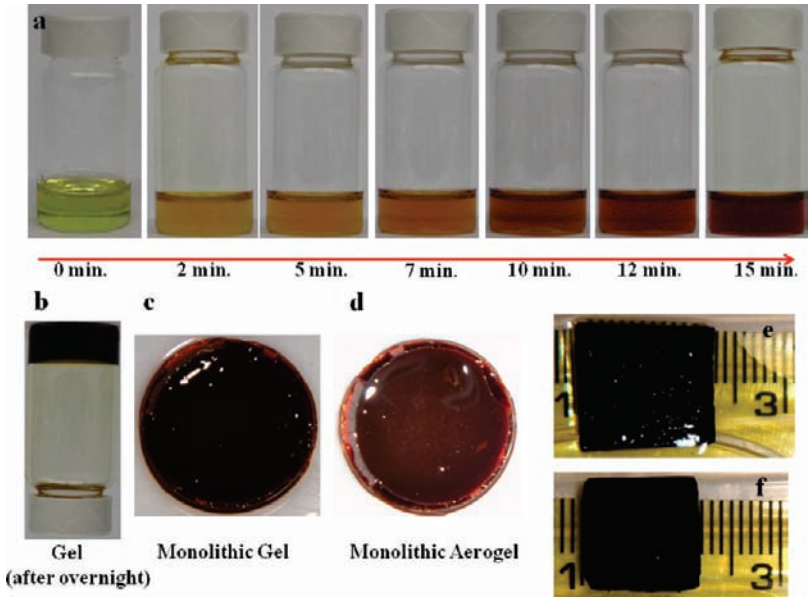

Figure 1. (a) Snapshots of $[SnS_4]^{4-}$ and Sb^{3+} during gelation. (b) Gel, (c) monolithic gel, and (d) aerogel from $[SnS_4]^{4-}$ and Sb^{3+} combination. (e) Monolithic gel and (f) aerogel from $[SbSe_4]^{3-}$ and Sb^{3+} combination.

colors become increasingly darker with time, indicating gradual polymerization and assembly of a metal−chalcogenide framework. Figure 1 demonstrates the color changes occurring in a solution containing $[SnS_4]^{4-}$ and antimony tartrate during gelation. Solvent exchange and supercritical CO_2 drying of the resultant alcogel gave aerogels. The final aerogels are very lightweight and adopt monolithic shapes and sizes that derive from the containers used for their synthesis. Chalcogel-Sb-4, for an example, possesses a bulk density of 0.1 g cm^{-3}. Seven different chalcogels were prepared and are listed in Table 1.

$$[SnS_4]^{4-} + \frac{4}{3}Sb^{3+} \rightarrow Sb_{4/3}[SnS_4] \quad (1)$$

$$[SbSe_4]^{3-} + Sb^{3+} \rightarrow Sb[SbSe_4] \quad (2)$$

$$[Sn_2S_6]^{4-} + 2Sn^{2+} \rightarrow Sn_2[Sn_2S_6] \quad (3)$$

The successful formation of gels from the chalcogenide clusters depends greatly on the synthetic conditions, the choice of suitable solvents, proper linking metal ions, and reaction temperature. The solubility of the precursor cluster and linking metal ion is the foremost criterion to be satisfied for making a gel. The reaction kinetics between linking metal ions and chalcogenide building blocks should be slow enough to avoid precipitation and permit a well-connected percolating medium to form during the process of gelation. To control the kinetics for gelation, we observed that it is important to select the proper ligands for the linking metal. For example, salts such as SbI_3 and $SbCl_3$ did not yield gels in either aqueous or nonaqueous solvents; instead they produced coagulates. The tartrate-chelated Sb^{3+} salt formed a monolithic gel in formamide with many chalcogenide clusters. The Sb^{3+} ions are slowly released from the chelating environment of the tartrate ligand and react with the chalcogenide building unit, forming the gel. Among the $[Sn_4Se_{10}]^{4-}$, $[Sn_2Se_6]^{4-}$, and $[SnSe_4]^{4-}$ series, gels were obtained with $[Sn_2Se_6]^{4-}$ and $[SnSe_4]^{4-}$ but not with $[Sn_4Se_{10}]^{4-}$. Even with a minimal amount of formamide present, in the case of $[Sn_4Se_{10}]^{4-}$ the solution remained clear, with no signs of gelation up to a month. Presumably, under the reaction conditions, the charge density on this larger cluster is not high enough to have proper attraction with Sb^{3+}, and thus no gel was obtained.

Similarly, the $[Ge_4Se_{10}]^{4-}$ and $[Ge_4S_{10}]^{4-}$ clusters did not yield monolithic rigid gels. Though the viscosity of the resulting solution increased gradually after the addition of the Sb^{3+} salt, apparently these units could not satisfy the proper charge density requirements with Sb^{3+} and failed to form rigid gels. However, the addition of equimolar quantities of Pt^{2+} and Sb^{3+} in the adamantane precursor solution did yield monolithic gels containing both Pt and Sb. This led to the new Chalcogel-PtSb-1 from $[Ge_4Se_{10}]^{4-}$.

The chemistry was further extended to acetate ligated Sn^{2+} salts, and monolithic gels were obtained with $[SnS_4]^{4-}$ and $[Sn_2S_6]^{4-}$. To make binary tin sulfide porous inorganic networks, $[SnS_4]^{4-}$ and $[Sn_2S_6]^{4-}$ building units were respectively linked with Sn^{2+} centers, resulting in Chalcogel-Sn-1 and Chalcogel-Sn-2.

Rheological Study. To test whether the charge density of the chalcogenide anions is important in making rigid chalcogels, *in situ* oscillatory shear linear viscoelastic property measurements were conducted on precursor solution during gelation. The rheology of polymeric networks is sensitive to structural changes within the liquid and thus often agrees well with the structure−property relationship in polymeric backbones.[40,44] In Figure 2a, the rheological parameter is the elastic storage modulus, G', which is a measure of the "stiffness" of the liquid and is plotted as a function of time for two different precursor solutions. As shown in Figure 2a, the two solutions behave drastically differently. The $[SnS_4]^{4-}$ anion, with higher negative charge density, readily reacts with antimony tartrate in formamide to increase its storage modulus with time (under 2% strain) and reaches a plateau of $G' \approx 600$ Pa after ~40 h. Under identical conditions, however, the elastic storage modulus of the $[Sn_2S_6]^{4-}/Sb^{3+}$−tartrate combination does not increase at all. This is consistent with the fact that the $[Sn_2S_6]^{4-}/Sb^{3+}$ system did not give gels. The shear-rate-dependent mechanical property

(44) Meng, J. R.; Hu, X.; Boey, F. Y. C.; Li, L. *Polymer* **2005**, *46*, 2766–2776.

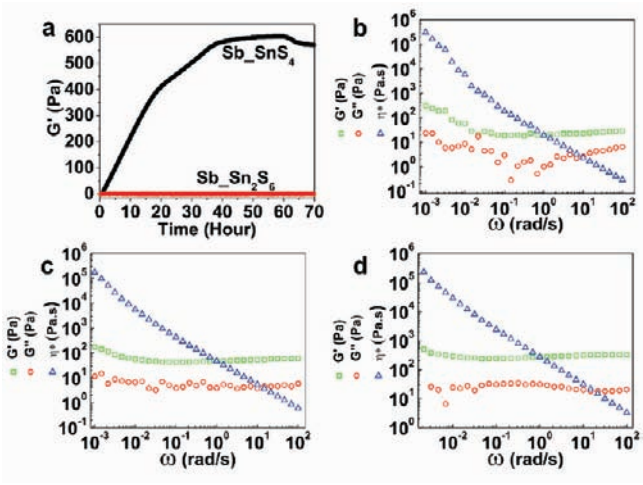

Figure 2. (a) Time-dependent storage moduli (G') of precursor sols containing antimony tartrate with $[SnS_4]^{4-}$ and $[Sn_2S_6]^{4-}$ building units separately. Frequency-dependent storage modulus (G'), loss modulus (G''), and complex viscosity (η^*) plots of Chalcogel-Sb-1 gelled for (b) 16 h, (c) 6 days, and (d) 6 weeks.

of Chalcogel-Sb-1 shows higher storage modulus (G') for 6-week-gelled sample compared to a sample gelled for a short time (e.g., 16 h or 6 day) at all frequencies. As the material becomes cross-linked to form the gel network, there is a rise in storage modulus, G'. This polymerization reaction consumes molecular species that otherwise would flow and contribute to the total energy loss. The less material that can flow, the lower the loss modulus, G'', and ultimately when the 3D assembly reaction is complete and there is no more reduction in material that can flow, the loss modulus will cease changing. Thus, G' successively increases from ~100 to ~300 to ~800 Pa for 16-h, 6-day, and 6-week-gelled samples, respectively, as shown in Figure 2 b−d. The shear-rate-dependent mechanical properties of the 6-week-gelled $[SnS_4]^{4-}$-containing sample are given in Figure 2d. The curves (Figure 2b−d) of the $[SnS_4]^{4-}$-containing sample indicate gel-like behavior, as the storage modulus (G') is independent of shear rate and significantly larger than the loss modulus (G''). Here, in each case the viscoelastic property of the mixture is dominated by elastic solid behavior. The magnitude of the complex viscosity, η^*, which is calculated from the measured storage (G') and loss (G'') moduli using Coxmerz's rule ($\eta^* = [(G'/\omega)^2 + (G''/\omega)^2]^{1/2}$),[40] shows a nonzero slope at all frequencies, indicating a percolated network. A decrease in η^* value with increasing frequency is interpreted as the destruction of network structures at higher frequency.

These results suggest that the high charge density of building units is a significant factor in forming Sb-based gels, although more experimentation is needed to ascertain this insight.

Measure of Pore Accessibility: Scanning Electron Microscopy. SEM images of the chalcogels show sponge-like interlinked porous particle morphology (Figure 3a,b). The smooth surface structure and absence of any dark phase on the ~50-μm-wide large particles suggest only a single phase is involved in the aerogel formation. Primary particles of nanometer size have aggregated together to form these large secondary particles of macroscopic size.[37] The fine, agglomerated surface structure of these materials is common throughout the entire series. In Figure 3c,d, three-dimensional laser confocal microscopy images of these aerogel samples demonstrate their rough surface and sponge-like morphology (average surface roughness, $R_z = 8-10$ μm).

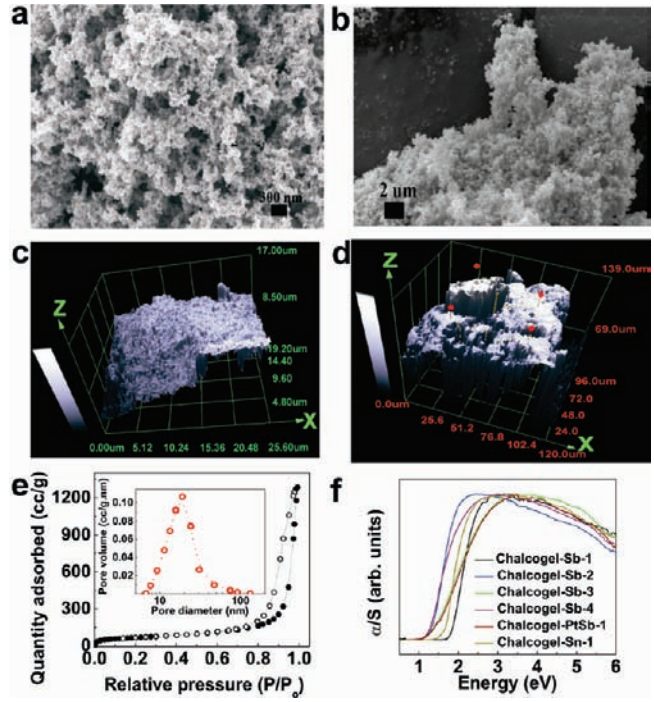

Figure 3. Scanning electron microscopy images of (a) Chalcogel-Sb-1 and (b) Chalcogel-Sb-4. Three-dimensional LEXT laser confocal microscopy images of (c) Chalcogel-Sb-1 and (d) Chalcogel-Sb-4. *x*, *y*, and *z* axes are sample length, width, and heighth, respectively. (e) Nitrogen adsorption−desorption isotherm of Chalcogel-Sb-1 at 77 K. The inset shows the BJH pore size distribution plot. (f) Ultraviolet−visible electronic adsorption spectra of aerogel samples.

Nitrogen Physisorption Analysis. The presence of pores in the chalcogel structures is reflected in their enormous surface area values obtained by applying the Brunauer−Emmett−Teller (BET)[45] model to nitrogen physisorption data at 77.15 K. The BET transform plot yields a high correlation coefficient of 0.999998 in the 0.05−0.2 relative pressure (P/P_0) region, suggesting validity of the multilayer model. Regardless of the chalcogenide building blocks and synthetic conditions, all chalcogels show a type-IV adsorption branch in the nitrogen isotherm curve (Figure 3e).[45] The presence of a combination of H1- and H3-type hysteresis loops indicates adsorption and desorption do not follow the same pathway, and significant fractions of cylindrical and slit-shape pore geometries are present.[45] This is a characteristic of interconnected mesoporous systems and has been observed in other chalcogenide aerogels.[6,7] The large volume uptake in the high relative pressure region and the absence of saturation in the adsorption isotherms are attributed to the condensation of molecules in large macropores.

Careful analysis of the isotherm data in the very low relative pressure region shows a type I isotherm, characteristic of microporous systems. The Barrett−Joynes−Halenda (BJH)[45] pore size distribution plot yields a wide range of pore sizes, starting from the micro (<2 nm size pores) to the meso (2−50 nm size pores) region. In order to quantify the percentage of microporosity in these chalcogels, the classical Dubinin−Radushkevich (DR)[45] pore-filling model was applied in the very low relative pressure region (P/P_0 from 0.00001 to 0.02, and around 27 points were fitted). The adsorption total pore volume, limiting micropore volume, and the percentage

(45) Gregg, S. J.; Sing, K. S. W. *Adsorption, Surface Area and Porosity*; Academic Press: New York, 1982.

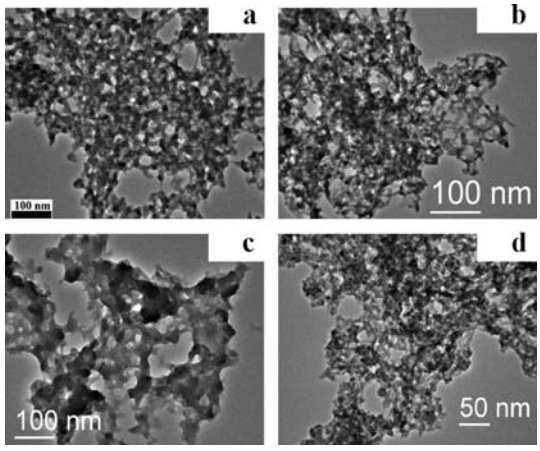

Figure 4. TEM images of supercritically dried (a) Chalcogel-Sb-1, (b) Chalcogel-Sb-4, (c) Chalcogel-Sn-2, and (d) Chalcogel-PtSb-1.

of microporosity of this series of chalcogels are presented in Table 1. The table shows that microporosity ranges from ∼6 to ∼20%, depending on the clusters and linking metal ions. The BJH pore size distribution plots obtained from different batches of Chalcogel-Sb-1 showed narrower pore size compared to the platinum-based chalcogel systems reported earlier (Figure 3e, inset).[6,7] We speculate that, during synthesis, the tartrate salt is acting as a template to direct the pore size to some extent. Surface areas obtained from these chalcogels are high, ranging from 114 to 368 m^2/g. Given that these chalcogels are composed of heavier elements and high skeletal densities, their surface areas per unit volume are very large. For example, Chalcogel-Sb-1 (skeletal density of 3.5 g/cm^3) possesses a BET surface area of 840 m^2/cm^3 and silica equivalent surface area of 821 m^2/g (per mol of chalcogel is converted into per mol of SiO_2 for equivalent surface area calculations).

Transmission Electron Microscopy. TEM shows that amorphous primary nanoparticles extensively aggregate to form secondary particles, and these secondary particles make meso- and macropores (see Figure 4). The "string of pearls", common in almost all TEM images, is made of nearly spherical interconnected colloidal nanoparticles of ∼20 nm size. This appears to be morphologically similar to the traditional base-catalyzed silica aerogels, where hydrolysis is the rate-determining step.[37] We presume that, as soon as the metal ion is released from the ligating environment, it immediately reacts with chalcogenide building units, and thus the rate is determined by the slow ligand substitution reaction. Both the antimony- and tin-containing chalcogels behave similarly in this respect.

Optical Properties. The chalcogels described here have relatively narrow energy band gaps and absorb light in the visible region. Depending on the chalcogenide building units and linking metal ions, the band gap varies from 1.30 eV (Chalcogel-Sb-2) to 1.88 eV (Chalcogel-Sb-1) (Table 1 and Figure 3f). In this series, the band gap values decrease from S to Se or from Ge to Sn as expected due to heavier Se or Sn compared to S or Ge.[6] Thus, the selenium-containing Chalcogel-Sb-2 has a lower band gap than the sulfur-containing analogue Chalcogel-Sb-1. The band gap energies obtained in this study lie in the same range as those of several important (e.g., InP, GaAs, CdSe, CdTe, etc.) semiconductors, suggesting possible interest for optoelectronic investigations.

Pair Distribution Function Analysis. To probe the local structures of the glassy chalcogels, the strong diffuse X-ray

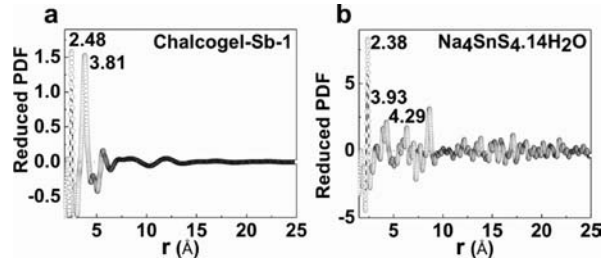

Figure 5. Reduced atomic pair distribution functions, $G(r)$, of (a) Chalcogel-Sb-1 and (b) precursor salt $Na_4SnS_4 \cdot 14H_2O$ as a function of interatomic distance r (Å).

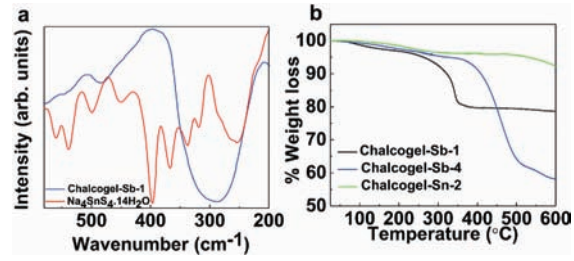

Figure 6. (a) Comparison of far-IR spectrum of Chalcogel-Sb-1 with that of the starting precursor. (b) TGA curves of Chalcogel-Sb-1 (black line), Chalcogel-Sb-4 (blue line), and Chalcogel-Sn-2 (green line) under nitrogen flow.

scattering displayed by these materials was analyzed using the PDF analysis technique.[46] The PDFs of the chalcogel samples show two strong correlation peaks corresponding to the first neighbor M−Q (M = main group metal, e.g., Sn or Ge or Sb; Q = S or Se) and second neighbor M···M/Q···Q/M···M′ distances. In Chalcogel-Sb-1, the first correlation peak, centered at 2.48 Å, arises from Sn−S or Sb−S bond distances (Figure 5a). In comparison, the same correlation peak in the precursor Na_4SnS_4 salt occurs at 2.38 Å, consistent with tetrahedral Sn−S bond distance (Figure 5b).[47] The second correlation peak, at 3.81 Å in Chalcogel-Sb-1, originates from second neighbor distances such as S···S and Sb···Sn. Because of the lack of well-defined orientational relationships between neighboring structural units, no observable correlation vectors were observed above 9 Å. The local order evident in the inorganic framework is also consistent with the infrared spectroscopic data (Figure 6a). Far-IR spectra of Chalcogel-Sb-1 show characteristic peaks in the same region as those of the $[SnS_4]^{4-}$ building unit. Sn−S stretching frequencies range from 200 to 500 cm^{-1} in the isolated $[SnS_4]^{4-}$ cluster.[48] However, because of the presence of different binding modes and the amorphous nature of the chalcogel, only a broad hump is observed in the far-IR region, and it is difficult to assign.

Thermal Stability. The sulfur-containing aerogel samples are markedly stable in air over time. The thermal stability of these solids was investigated with thermogravimetric analysis (TGA) (Figure 6b). These compounds show no appreciable weight loss up to at least 250 °C. In this temperature range, the small weight loss, ∼5−10% depending on the sample, is caused by the evaporation of physisorbed or chemisorbed solvent left in the

(46) Billinge, S. J. L.; Kanatzidis, M. G. *Chem. Commun.* **2004**, 749–760.
(47) Willett, R. D.; Vij, A.; Imhof, J. M.; Cleary, D. A. *J. Chem. Crystallogr.* **2000**, *30*, 405–410.
(48) Jia, D. X.; Zhang, Y.; Dai, J.; Zhu, Q. Y.; Gu, X. M. *Z. Anorg. Allg. Chem.* **2004**, *630*, 313–318.

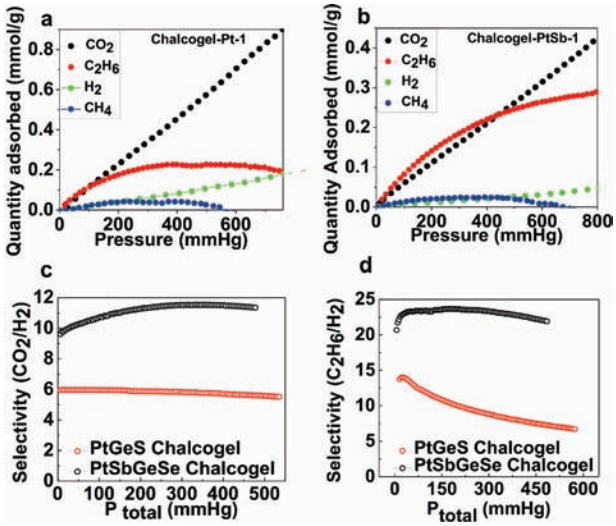

Figure 7. Adsorption isotherms of CO_2, C_2H_6, H_2, and CH_4 on (a) Chalcogel-Pt-1 (PtGeS) and (b) Chalcogel-PtSb-1 (PtSbGeSe) at 273 K. (c,d) Comparison of gas selectivity (CO_2 and C_2H_6 versus H_2) plots between Chalcogel-PtSb-1 (PtSbGeSe) and Chalcogel-Pt-1 (PtGeS).

random networks. After that, rapid weight loss results from the removal of chalcogen; however, Chalcogel-Sn-2 showed thermal stability up to 450 °C without major weight loss.

Selective Gas Adsorption. Because of the presence of heavy "soft" elements in these structures, the accessible pore surfaces are expected to be electronically more polarizable than, for example, oxide surfaces.[49] Previous findings with ordered mesoporous Ge_9Q_x (Q = S, Se, Te) materials showed selective adsorption of gases which scaled with the polarizability of the gas molecules.[49b] This led us to test the title chalcogel materials for their ability to differentiate among various gases on the basis of their polarizability. The adsorption isotherms of the aerogel samples show a higher uptake of polarizable gases such as CO_2 and CH_3CH_3 compared to the less polarizable H_2 and CH_4 [polarizability (α): $\alpha(CH_3CH_3) = 4.43 > \alpha(CO_2) = 2.91 > \alpha(CH_4) = 2.59 > \alpha(H_2) = 0.80$ (in units of 10^{-24} cm^3)][50a] (Figure 7a,b).

In order to correlate the adsorption property with surface functionality, two representative aerogel samples are compared: the sulfide Chalcogel-Pt-1 ($Pt_2Ge_4S_{10}$)[6] and the selenide Chalcogel-PtSb-1 (PtSbGeSe). The major difference between the two samples is their surface polarizability. The presence of heavier selenium atoms renders the surface of Chalcogel-PtSb-1 more polarizable, and this is reflected in its selectivity toward gases. Analysis of gas selectivity using IAST[43] from single-component isotherms showed almost a 2-fold increase in selectivity values (both CO_2/H_2 and CH_3CH_3/H_2) for Chalcogel-PtSb-1 compared to Chalcogel-Pt-1 at 1 atm and 273 K (Figure 7c,d). Calculated values for the selenium-containing samples are of the same order of magnitude as for mesoporous NU-GeSe-1.[49b] Even though the calculated selectivities of our present chalcogel samples are lower than those of the best mesoporous Ge_9Q_x (Q = S, Se, Te) materials, our current experimentation suggests that, with further modification of the inorganic frameworks and their pore structure, even better selectivities could be achieved in these chalcogel systems. Materials that exhibit high CO_2/H_2 selectivity are organic polymeric membranes ($S_{CO_2/H_2} \approx 31$), high-performance ceramic membranes ($S_{CO_2/H_2} \approx 60-110$), and zeolites.[50b−d] However, they usually possess a complex structure and often show diffusivity and/or a combination of both diffusivity and solubility selectivity. In these cases as well, it is possible that the same polarizability effect is present and can explain the CO_2 selectivity.

Concluding Remarks

Slow framework assembly reactions between $[MQ_4]^{4-}$, $[M_2Q_6]^{4-}$, and $[MQ_4]^{3-}$ anions and metal complexes appear to be crucial in achieving gelation and forming chalcogels. This is achieved by chelating the metal ions with organic ligands such as tartrate or acetate in formamide. The use of tartrate-ligated metal salts in nonaqueous solvents yields rigid chalcogels that are transformed into porous aerogels after supercritical drying. We have shown that a wide variety of main-group metal ions can be successfully employed in chalcogel synthesis if proper synthetic conditions are employed, and even quaternary aerogels can be produced. *In situ* rheological studies suggest that a high charge density on the building chalcogenide units favors more rigid gel structures, while fragile gels are obtained from low-charged building units. The high surface polarizability of the inorganic network plays an important role in the selective adsorption of gas molecules like CO_2 and C_2H_6 by the chalcogels. A further improvement in chalcogel gas selectivity is anticipated by incorporating even heavier polarizable elements into the inorganic frameworks. This indicates that these systems may have a significant impact in gas separation processes.

Our current results along with previous studies suggest metathesis chemistry is indeed a general pathway for creating wide varieties of porous, semiconducting aerogels. Since silica aerogels have the benefit of decades long research, doping and surface modifications similar to those possible for silica at the pre- and postgelation stage could be envisioned in these new chalcogenide frameworks. Nanoporous tin sulfides made by Ozin et al. show unique thermochemical properties and band gap sensitivity to guest molecule adsorption.[51,52] Also R-SnS-n-type materials (R represents occluded organic cations) show unique sensing properties toward guest molecules through a response in drastic electrical property change.[53] The chalcogels could add to these properties through their very high surface areas, which could enable facile incorporation of a variety of guest species into their structures. Finally, the solution-based gelation and aerogel formation processes should allow for the deposition of cast films for a variety of experiments and uses including sensing, gas absorption, chemical remediation and separation, catalysis, supercapacitors, solid-state devices, etc.

Acknowledgment. These studies were supported primarily by the Nanoscale Science and Engineering Initiative of the

(49) (a) Shanker, J.; Agrawal, S. C.; Lashkari, A. K. G. *Solid State Commun.* **1978**, *26*, 675–677. (b) Armatas, G. S.; Kanatzidis, M. G. *Nat. Mater.* **2009**, *8*, 217–222.
(50) (a) *CRC Handbook of Chemistry and Physics*, 81st ed.; CRC Press: New York, 2000. (b) Lin, H.; Wagner, E. V.; Freeman, B. D.; Toy, L. G.; Gupta, R. P. *Science* **2006**, *311*, 639–642. (c) Verweij, H.; Lin, Y. S.; Dong, J. *MRS Bull.* **2006**, *31*, 756–764. (d) Ockwig, N. W.; Nenoff, T. M. *Chem. Rev.* **2007**, *107*, 4078–4110.
(51) Ahari, H.; Bowes, C. L.; Jiang, T.; Lough, A.; Ozin, G. A.; Bedard, F. L.; Petrov, S.; Young, D. *Adv. Mater.* **1995**, *7*, 375–378.
(52) Jiang, T.; Ozin, G. A.; Bedard, R. L. *Adv. Mater.* **1995**, *7*, 166–170.
(53) Jiang, T.; Ozin, G. A.; Verma, A.; Bedard, R. L. *J. Mater. Chem.* **1998**, *8*, 1649–1656.

National Science Foundation under NSF Award Number EEC-0647560. We are also thankful to Dr. Peter J. Chupas at Argonne National Laboratory for collection of PDF data. We acknowledge Saswati Pujari and Prof. Wesley R. Burghardt of the Department of Chemical and Biological Engineering at Northwestern University for help with the rheological measurements. ICP-AES measurements were performed using Analytical Service Laboratory facilities at Northwestern University. Electron microscopy images were taken using the facilities of the NUANCE at Northwestern.

Supporting Information Available: Large-angle powder X-ray diffraction data, nitrogen adsorption−desorption isotherm, and pore size distribution. This material is available free of charge via the Internet at http://pubs.acs.org.

JA1059284